J. Mech. Phys. Solids 206 (2026) 106383

Contents lists available at ScienceDirect

Journal of the Mechanics and Physics of Solids

journal homepage: www.elsevier.com/locate/jmps

Flexible filaments in vesicles with reduced volume: Anisotropic confinement and morphological response

Chao Shi[1], Chengyao Zhang[1], Yaxin Fang, Xin Yi *

School of Mechanics and Engineering Science, Peking University, Beijing 100871, China

ARTICLE INFO

Keywords:
Filament–vesicle system
Flexible confinement
Anisotropic confinement
Morphological transitions
Instability

ABSTRACT

The mechanical interplay between cell membranes and enclosed filaments is central to various cellular activities, particularly cellular morphogenesis. Here, we present a theoretical study of filament loop-induced shape transformations in vesicles with varying reduced volumes, emphasizing the coupling among filament elasticity, membrane deformability, and anisotropic confinement. We identify a range of morphological transitions—including filament buckling and reorientation, prolate-to-oblate vesicle shape changes, and complex symmetry breaking—governed by relative filament stiffness, length, and vesicle volume. Morphological phase diagrams are constructed, and energy analysis reveals the underlying mechanisms of shape transformations. We further characterize the evolution of membrane tension and examine the packing behavior of inhomogeneous filament loops. The results are complemented by a conceptually driven discussion of how anisotropic confinement and filament–vesicle coupling shape morphogenetic behavior. Our findings provide physical insight into filament–vesicle mechanics, with implications for cell shaping, cytoskeletal organization, and the design of filament-based artificial cells.

1. Introduction

Confinement is a key driver of symmetry breaking and structural reorganization in mechanical and biological systems. In many cellular contexts, the confinement is soft—the enclosing boundary is deformable and responds to internal forces or external stimuli. A prominent example is the cell membrane, which reshapes under forces from internal cytoskeletal filaments or external mechanical cues. This boundary flexibility allows cells to adapt their morphology during migration, division, or deformation, as in red blood cells and invasive cancer cells (Bray, 2000; Blanchoin et al., 2014; Alves et al., 2025). At the core of these processes lies a bidirectional mechanical coupling: cytoskeletal filaments deform the membrane, while the membrane imposes geometric and mechanical constraints that regulate filament organization. Understanding this interplay is essential for elucidating the mechanics of morphogenesis, motility, and intracellular transport in both living and synthetic cells. A common model of synthetic cells consists of lipid vesicles enclosing biofilaments, serving as minimal systems designed to mimic selected structural, functional, or dynamic features of living cells.

Filamentous structures under membrane confinement span a continuum of topologies—from open filaments (e.g., individual actin or microtubule segments) to closed filament loops (e.g., contractile actin rings) and interconnected networks forming structural scaffolds. For example, elongating microtubule-based mitotic spindles buckle within nuclei when nuclear envelope expansion is restricted, underscoring the role of deformable confinement in preserving spindle function (Yam et al., 2011). Open filaments in

* Corresponding author.
E-mail address: xyi@pku.edu.cn (X. Yi).
[1] C.S. and C.Z. contributed equally to this work.

https://doi.org/10.1016/j.jmps.2025.106383
Received 21 June 2025; Received in revised form 14 August 2025; Accepted 27 September 2025
Available online 4 October 2025

vesicles can induce diverse vesicle morphologies—oblate, dumpling, lemon, cherry, pebble, droplet, or racket-like—depending on their relative stiffness and length (Fygenson et al., 1997; Tsai and Koenderink, 2015; Zou et al., 2018; Wu et al., 2019; Behera et al., 2020; Shi et al., 2023). Membrane-bound filaments such as dynamin, ESCRT-III, and Atg17 complexes further illustrate how filament–membrane coupling enables diverse membrane remodeling processes, including fission (McDargh et al., 2016; Ganichkina et al., 2021), scission (Meadowcroft et al., 2022), and autophagy (Bahrami et al., 2017).

Unlike open filaments, closed loops and interconnected filamentous networks—e.g., marginal bands in platelets (Diagouraga et al., 2014; Dmitrieff et al., 2017), FtsZ rings in bacteria (Szwedziak et al., 2014), actomyosin rings in cells and vesicles (Miyazaki et al., 2015; Litschel et al., 2021), and actin and microtubule networks in vesicles (Litschel et al., 2021; Bashirzadeh et al., 2021)—are topologically constrained, prohibiting local relaxation through filament end displacement or by translating and rotating. This closure feature promotes cooperative deformation across the entire filament structure and amplifies confinement-induced geometric frustration, leading to complex filament packing, including in-plane and out-of-plane buckling and symmetry breaking. For instance, closed filament loops with varying lengths and stiffnesses exhibit transitions among circular, oval, saddle-shaped, and figure-eight configurations within vesicles (Limozin and Sackmann, 2002; Tsai and Koenderink, 2015; Shi et al., 2023), reflecting strong filament–membrane interplay. A similar buckling transition occurs during platelet activation: the marginal band, a planar microtubule loop that stabilizes the discoid shape in resting platelets, buckles into a saddle-like configuration as the cell rounds into a sphere upon biochemical activation (Diagouraga et al., 2014; Dmitrieff et al., 2017). In actin-based cytoskeleton-vesicle systems, high actin concentrations promote the formation of short, dense bundles that assemble into interconnected, spiderweb-like networks, stabilizing the vesicle. In contrast, at low actin concentrations, long, bent bundles align along the membrane, often forming ring-like structures (Litschel et al., 2021). Blood clots offer another biologically relevant example, comprising entangled fibrin filament networks interwoven with deformable red blood cells, forming soft yet mechanically resilient composites (Filla et al., 2024; Gu et al., 2025).

Beyond biological contexts, related confinement-induced morphological transitions arise in physical systems such as thin rod packing inside elastic shells. Depending on friction, loop length, and shell stiffness, long elastic rod loops adopt spiral, classical, folded, or warped morphologies via bifurcation instabilities, accompanied by shell deformation (Vetter et al., 2014). While differing in setting and function, these systems provide valuable analogies that motivate a broader inquiry into how confinement elasticity and filament mechanics jointly shape emergent structures.

Despite this relevance across disciplines such as cellular mechanics, synthetic biology, and packing engineering, the mechanical principles governing elastic filaments under elastic confinement — particularly closed flexible loops within deformable vesicles — remain poorly understood. Most theoretical studies of closed loops focus on either rigid filaments (Vázquez-Montejo et al., 2025) or rigid confinements (e.g., spherical, cylindrical, or ellipsoidal) (Guven and Vázquez-Montejo, 2012; Vázquez-Montejo et al., 2015; Dmitrieff et al., 2017; Tortora and Jost, 2023; Wang et al., 2024), with only a few examining flexible loops inside vesicles without systematically accounting for volume constraints (Shi et al., 2023; Zhang et al., 2024). Yet vesicle volume profoundly affects membrane morphology (Seifert et al., 1991) and interaction with attaching entities such as nanoparticles or membrane-associated proteins (Bahrami et al., 2017). A fixed volume forces the vesicles into nonspherical shapes, imposing anisotropic confinement on the enclosed filaments, specifically by introducing stronger geometric constraints along certain directions than others. These directional constraints modify the filaments' accessible configuration space and bias their buckling and reorientation pathways, favoring symmetry-breaking morphologies. While axisymmetric or mirror-symmetric configurations may still emerge, anisotropic confinement enables a broader range of mechanically stable, structurally distinct states.

Here, we theoretically investigate vesicle morphogenesis driven by confined filament loops, emphasizing the combined effects of vesicle volume and filament stiffness and size on system morphology, highlighting the interplay between filament mechanics and volume-constrained soft confinement. The resulting shape transformations are captured in symmetry-based phase diagrams. By analyzing system energy, membrane tension, pressure difference, and internal filament forces, we reveal the mechanical pathways underlying these transitions. We further examine how inhomogeneous filaments with segmental stiffness modulate vesicle shape. This work presents a conceptually clean and physically grounded continuum model for understanding mechanically driven morphological changes in confined filament–vesicle systems, relevant to cellular mechanics and biomimetic design.

2. Theoretical modeling

Consider an inextensible filament loop of total length L enclosed in a lipid vesicle (Fig. 1). The vesicle has a fixed surface area $A(=4\pi R^2)$ and a specified reduced volume $v = V/(4\pi R^3/3)$, where R is the effective vesicle radius and V is the vesicle volume. Based on the Helfrich membrane theory for the vesicle membrane (Helfrich, 1973) and the wormlike chain model for the filament (Doi and Edwards, 1986), the total system energy $E_{\rm tot} = E_{\rm m} + E_{\rm f}$ comprises the bending energy $E_{\rm m}$ of the vesicle membrane of zero spontaneous curvature and the filament bending energy $E_{\rm f}$ described as

$$E_{\rm m} = 2\kappa \int H^2 \,{\rm d}A, \quad E_{\rm f} = \frac{YI}{2}\int_0^L C^2 \,{\rm d}s.$$

Here, κ, H, and ${\rm d}A$ represent the bending rigidity, local mean curvature, and surface element of the membrane, respectively; YI (Y as the Young's modulus and I as the moment of inertia), C, and ${\rm d}s$ denote the bending stiffness, local curvature, and length element of the filament, respectively. By rescaling all length scales by R and all energy scales by κ, the system behavior is governed by the relative stiffness and length of the filament to the vesicle, as well as the reduced vesicle volume v, such that $E_{\rm tot} = E_{\rm tot}\,(YI/(\kappa R),\, L/R,\, v)$.

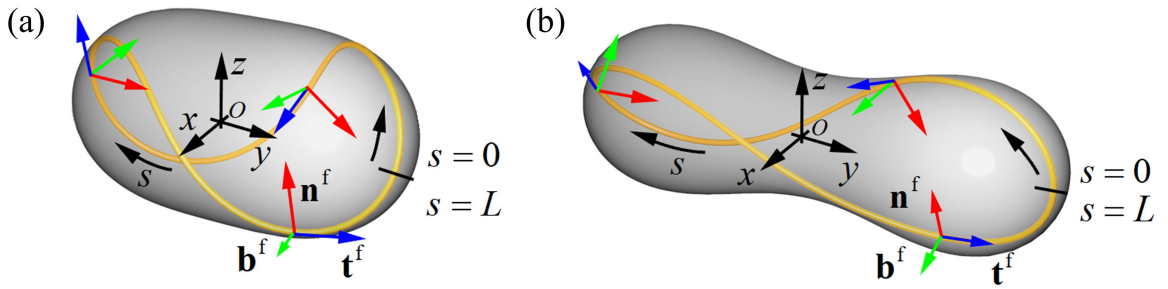

Fig. 1. Schematic of an inextensible filament loop of length L enclosed in a lipid vesicle of given reduced volume v. (a) Convex vesicle at $v = 0.9$, and (b) concave vesicle at $v = 0.7$. The Frenet frame $\{\mathbf{t}^{\mathrm{f}}, \mathbf{n}^{\mathrm{f}}, \mathbf{b}^{\mathrm{f}}\}$, comprising the unit tangent vector $\mathbf{t}^{\mathrm{f}}$, unit normal vector $\mathbf{n}^{\mathrm{f}}$, and unit binormal vector $\mathbf{b}^{\mathrm{f}}$, is defined along the filament loop, with s denoting the filament arclength. The origin O of the adopted Cartesian coordinate system (x, y, z) is positioned within the vesicle.

To capture the complex configurations of the vesicle, we employ the spherical harmonics representation to parameterize the position vector $\mathbf{r}^{\mathrm{m}}$ of the vesicle membrane in a Cartesian coordinate system as (Khairy and Howard, 2011; Shi et al., 2023)

$$\mathbf{r}^{\mathrm{m}}(\theta,\varphi) = \begin{bmatrix} x^{\mathrm{m}}(\theta,\varphi) \\ y^{\mathrm{m}}(\theta,\varphi) \\ z^{\mathrm{m}}(\theta,\varphi) \end{bmatrix} = \begin{bmatrix} \sum_{l=0}^{l_{\max}} \sum_{k=-l}^{l} C_{lk}^{x}\, y_{lk}(\theta,\varphi) \\ \sum_{l=0}^{l_{\max}} \sum_{k=-l}^{l} C_{lk}^{y}\, y_{lk}(\theta,\varphi) \\ \sum_{l=0}^{l_{\max}} \sum_{k=-l}^{l} C_{lk}^{z}\, y_{lk}(\theta,\varphi) \end{bmatrix},$$

where $\theta \in [0,\pi]$ and $\varphi \in [0,2\pi]$ represent the polar and azimuthal angles in a spherical coordinate system, respectively. C_{lk}^{x}, C_{lk}^{y}, and C_{lk}^{z} are the coefficients, and $y_{lk}(\theta,\varphi)$ is the real spherical harmonics, indexed by the integers l and k, as

$$y_{lk}(\theta,\varphi) = \begin{cases} \sqrt{2} M_{lk} P_{lk}(\cos\theta)\cos(k\varphi), & \text{if } k > 0, \\ M_{l0} P_{l0}(\cos\theta), & \text{if } k = 0, \\ \sqrt{2} M_{lk} P_{lk}(\cos\theta)\sin(-k\varphi), & \text{if } k < 0, \end{cases}$$

where

$$M_{lk} = \sqrt{\frac{(2l+1)(l-|k|)!}{4\pi(l+|k|)!}} \quad \text{and} \quad P_{lk}(x) = \frac{(-1)^{|k|}}{2^l l!}(1-x^2)^{|k|/2}\frac{\mathrm{d}^{l+|k|}}{\mathrm{d}x^{l+|k|}}[(x^2-1)^l].$$

With the parameterized form of $\mathbf{r}^{\mathrm{m}}(\theta,\varphi)$, geometrical properties of the vesicle can be derived using classical differential geometry (Kreyszig, 1991). For example, the unit normal vector to the vesicle surface is

$$\mathbf{n}^{\mathrm{m}} = \frac{\mathbf{r}^{\mathrm{m}}_{,\theta} \times \mathbf{r}^{\mathrm{m}}_{,\varphi}}{|\mathbf{r}^{\mathrm{m}}_{,\theta} \times \mathbf{r}^{\mathrm{m}}_{,\varphi}|},$$

where the comma in the subscript denotes partial differentiation with respect to the indicated coordinate hereinafter (e.g., $\mathbf{r}^{\mathrm{m}}_{,\theta} \equiv \partial\mathbf{r}^{\mathrm{m}}/\partial\theta$ and $\mathbf{r}^{\mathrm{m}}_{,\theta\varphi} \equiv \partial^2\mathbf{r}^{\mathrm{m}}/\partial\theta\partial\varphi$).

Introducing the first and second fundamental form coefficients $E = \mathbf{r}^{\mathrm{m}}_{,\theta} \cdot \mathbf{r}^{\mathrm{m}}_{,\theta}$, $F = \mathbf{r}^{\mathrm{m}}_{,\theta} \cdot \mathbf{r}^{\mathrm{m}}_{,\varphi}$, $G = \mathbf{r}^{\mathrm{m}}_{,\varphi} \cdot \mathbf{r}^{\mathrm{m}}_{,\varphi}$, $L = \mathbf{r}^{\mathrm{m}}_{,\theta\theta} \cdot \mathbf{n}^{\mathrm{m}}$, $M = \mathbf{r}^{\mathrm{m}}_{,\theta\varphi} \cdot \mathbf{n}^{\mathrm{m}}$, and $N = \mathbf{r}^{\mathrm{m}}_{,\varphi\varphi} \cdot \mathbf{n}^{\mathrm{m}}$, the local mean curvature H of the vesicle surface is

$$H = \frac{EN + GL - 2FM}{2(EG - F^2)}.$$

Then the bending energy of the vesicle membrane is

$$E_{\mathrm{m}} = 2\kappa \int H^2 \,\mathrm{d}A = 2\kappa \int_0^{2\pi}\int_0^{\pi} H^2 \sqrt{EG - F^2}\,\mathrm{d}\theta\mathrm{d}\varphi, \tag{1}$$

where the vesicle area element $\mathrm{d}A = |\mathbf{r}^{\mathrm{m}}_{,\theta} \times \mathbf{r}^{\mathrm{m}}_{,\varphi}|\,\mathrm{d}\theta\mathrm{d}\varphi$ has been used.

The vesicle area A and vesicle volume V are given by the following expressions, respectively:

$$A = \int_0^{2\pi}\int_0^{\pi} \left|\mathbf{r}^{\mathrm{m}}_{,\theta} \times \mathbf{r}^{\mathrm{m}}_{,\varphi}\right| \mathrm{d}\theta\mathrm{d}\varphi \quad \text{and} \quad V = \frac{1}{3}\int_0^{2\pi}\int_0^{\pi} \mathbf{r}^{\mathrm{m}} \cdot (\mathbf{r}^{\mathrm{m}}_{,\theta} \times \mathbf{r}^{\mathrm{m}}_{,\varphi})\,\mathrm{d}\theta\mathrm{d}\varphi.$$

The confined filament bends against the vesicle membrane and is assumed to be constrained on the inner surface of the vesicle. Due to the lateral mobility of lipid molecules in the vesicle membrane, the filament can slip freely along the surface over long

timescales. These constraints allow the filament's position vector to be parameterized as $\mathbf{r}^{\mathrm{f}}(\varphi) = \mathbf{r}^{\mathrm{m}}(\theta_0, \varphi)$, where θ_0 is a prescribed constant polar angle. A similar compatibility scheme coupling the filament with the membrane has been employed to investigate the configurations of the filament–vesicle system, where the membrane is discretized as a fluid shell using the Helfrich energy, and the filament is modeled as a Cosserat rod (Sharma et al., 2023). Then using classical differential geometry (Kreyszig, 1991), the filament geometrical properties can be obtained. For the filament, whose centerline curve is parameterized by $\mathbf{r}^{\mathrm{f}}(\varphi)$, its unit tangent vector $\mathbf{t}^{\mathrm{f}}(\varphi)$, unit principal normal vector $\mathbf{n}^{\mathrm{f}}(\varphi)$, and unit binormal vector $\mathbf{b}^{\mathrm{f}}(\varphi)$ are given as

$$\mathbf{t}^{\mathrm{f}}(\varphi) = \frac{\mathbf{r}^{\mathrm{f}}_{,\varphi}}{|\mathbf{r}^{\mathrm{f}}_{,\varphi}|}, \quad \mathbf{n}^{\mathrm{f}}(\varphi) = \frac{\mathbf{r}^{\mathrm{f}}_{,\varphi} \times \mathbf{r}^{\mathrm{f}}_{,\varphi\varphi}}{|\mathbf{r}^{\mathrm{f}}_{,\varphi} \times \mathbf{r}^{\mathrm{f}}_{,\varphi\varphi}|}, \quad \text{and} \quad \mathbf{b}^{\mathrm{f}}(\varphi) = \mathbf{t}^{\mathrm{f}} \times \mathbf{n}^{\mathrm{f}} = \frac{|\mathbf{r}^{\mathrm{f}}_{,\varphi}|}{|\mathbf{r}^{\mathrm{f}}_{,\varphi} \times \mathbf{r}^{\mathrm{f}}_{,\varphi\varphi}|}\, \mathbf{r}^{\mathrm{f}}_{,\varphi\varphi} - \frac{\mathbf{r}^{\mathrm{f}}_{,\varphi} \cdot \mathbf{r}^{\mathrm{f}}_{,\varphi\varphi}}{|\mathbf{r}^{\mathrm{f}}_{,\varphi}| \cdot |\mathbf{r}^{\mathrm{f}}_{,\varphi} \times \mathbf{r}^{\mathrm{f}}_{,\varphi\varphi}|}\, \mathbf{r}^{\mathrm{f}}_{,\varphi}.$$

The vectors $\mathbf{t}^{\mathrm{f}}$, $\mathbf{n}^{\mathrm{f}}$, and $\mathbf{b}^{\mathrm{f}}$ form a right-handed orthogonal trihedron along the filament centerline curve. The vector arrangement, $\{\mathbf{r}^{\mathrm{f}};\ \mathbf{t}^{\mathrm{f}},\ \mathbf{n}^{\mathrm{f}},\ \mathbf{b}^{\mathrm{f}}\}$, is known as the Frenet frame (Fig. 1).

The local curvature C and torsion T of the filament are given as

$$C = \frac{|\mathbf{r}^{\mathrm{f}}_{,\varphi} \times \mathbf{r}^{\mathrm{f}}_{,\varphi\varphi}|}{|\mathbf{r}^{\mathrm{f}}_{,\varphi}|^3} \quad \text{and} \quad T = \frac{(\mathbf{r}^{\mathrm{f}}_{,\varphi} \times \mathbf{r}^{\mathrm{f}}_{,\varphi\varphi}) \cdot \mathbf{r}^{\mathrm{f}}_{,\varphi\varphi\varphi}}{|\mathbf{r}^{\mathrm{f}}_{,\varphi} \times \mathbf{r}^{\mathrm{f}}_{,\varphi\varphi}|^2},$$

and the filament bending energy is

$$E_{\mathrm{f}} = \frac{YI}{2} \int_0^L C^2 \, \mathrm{d}s = \frac{YI}{2} \int_0^{2\pi} \frac{|\mathbf{r}^{\mathrm{f}}_{,\varphi} \times \mathbf{r}^{\mathrm{f}}_{,\varphi\varphi}|^2}{|\mathbf{r}^{\mathrm{f}}_{,\varphi}|^5} \, \mathrm{d}\varphi, \tag{2}$$

where the filament length element is $\mathrm{d}s = |\mathbf{r}^{\mathrm{f}}_{,\varphi}| \, \mathrm{d}\varphi$.

The filament length is $L = \int_0^{2\pi} |\mathrm{d}\mathbf{r}^{\mathrm{f}}/\mathrm{d}\varphi| \, \mathrm{d}\varphi$.

Combining Eqs. (1) and (2), the total system energy is $E_{\mathrm{tot}}(C^x_{lk}, C^y_{lk}, C^z_{lk}) = E_{\mathrm{m}} + E_{\mathrm{f}}$, expressed as a function of the control coefficients C^x_{lk}, C^y_{lk}, and C^z_{lk}. A total number of the control coefficients is $3(l_{\max}+1)^2$. We set $l_{\max} = 5$ in our calculations. Given energy E_{tot}, equality constraints for vesicle area A, reduced volume v, and filament length L^{f}, and their respective first derivatives with respect to the control points, the system's minimum energy state at specified $YI/(\kappa R)$ and L/R is determined using the sequential quadratic programming method for constrained optimization (Fletcher, 1987). As a result, the corresponding vesicle shape $\mathbf{r}^{\mathrm{m}}(\theta, \varphi)$ and filament configuration $\mathbf{r}^{\mathrm{f}}(\varphi)$ are obtained.

Once the geometric properties of both the filament and vesicle surface are determined, the forces acting on the surface-constrained filament can be derived using balance equations for local forces and moments (Wang and Yi, 2024). In general, the internal force $\mathbf{F}$ of the filament is

$$\mathbf{F} = YI \left[\left(\beta - \frac{C^2}{2} \right) \mathbf{t}^{\mathrm{f}} - C' \mathbf{n}^{\mathrm{f}} - CT \mathbf{b}^{\mathrm{f}} \right], \tag{3}$$

where β is a constant Lagrange multiplier globally enforcing filament inextensibility, determined through the constrained optimization. The primes in Eqs. (3) and (4) denote derivatives with respect to the filament arclength s and can be converted to derivatives with respect to the azimuthal angle φ via the chain rule using $\mathrm{d}s/\mathrm{d}\varphi = |\mathbf{r}^{\mathrm{f}}_{,\varphi}|$. Alternatively, for the filament segment with non-vanishing geodesic curvature, the filament internal force is $\mathbf{F} = F_{\mathrm{t}}\mathbf{t}^{\mathrm{f}} + F_{\mathrm{n}}\mathbf{n}^{\mathrm{f}} + F_{\mathrm{b}}\mathbf{b}^{\mathrm{f}}$ with force components (Wang and Yi, 2024)

$$F_{\mathrm{t}} = YI \left[\frac{C''}{C} - T^2 - \frac{C_{\mathrm{n}}}{C_{\mathrm{g}}} \left(2\frac{C'}{C} T + T' \right) \right], \quad F_{\mathrm{n}} = -YIC', \quad F_{\mathrm{b}} = -YICT, \tag{4}$$

where $C_{\mathrm{n}} = C\mathbf{n}^{\mathrm{m}} \cdot \mathbf{n}^{\mathrm{f}}$ and $C_{\mathrm{g}} = C\mathbf{n}^{\mathrm{m}} \cdot \mathbf{b}^{\mathrm{f}}$ are the normal curvature and geodesic curvature of the filament curve, respectively.

For the filament segment with zero geodesic curvature ($C_{\mathrm{g}} = 0$), the force balance along the tangent $\mathbf{t}^{\mathrm{f}}$ gives $F'_{\mathrm{t}} = CF_{\mathrm{n}} = -YICC'$ (Wang and Yi, 2024). Integrating F'_{t} from a reference position $s = s^*$, where the geodesic curvature is nonzero or the tangential force is known, allows us to determine $F_{\mathrm{t}}(s)$ as

$$F_{\mathrm{t}}(s) = -YI \int_{s^*}^{s} CC' \, \mathrm{d}s + F_{\mathrm{t}}(s^*). \tag{5}$$

3. Results on system morphologies and force properties with homogeneous filaments

Depending on the value of the reduced vesicle volume v, a filament-free vesicle adopts various shapes. At $v = 1$, the vesicle remains spherical, while at lower volumes it transitions through prolate ($v \in (0.651, 1)$), oblate ($v \in (0.591, 0.651)$), and stomatocyte ($v \in (0, 0.591)$) configurations (Seifert et al., 1991). These nonspherical vesicle shapes impose anisotropic confinement on the filaments. Conversely, the introduction of filaments can alter the degree of anisotropy of the vesicle. To elucidate how the intrinsic shape of the vesicle confinement influences the filament–vesicle interaction, and how the confined filaments, in turn, affect vesicle morphology, detailed analyses are conducted for $v = 0.9$ and 0.7. At $v = 0.9$, a filament-free vesicle maintains a convex prolate shape (prolate ellipsoid), whereas at $v = 0.7$, it adopts a concave dumbbell-like shape with two spheroidal lobes (prolate dumbbell). In this section, we focus on systems with homogeneous filaments exhibiting uniform bending stiffness. The effects of filament inhomogeneity on system behavior are explored in Section 4.

3.1. The filament–vesicle system at a reduced volume of $v = 0.9$

We first examine the mechanical interplay between the filament loop and the vesicle at $v = 0.9$. Fig. 2a-f presents representative system configurations obtained via numerical optimization for selected values of normalized filament bending stiffness $YI/(\kappa R)$ and filament length L/R. A diverse array of rich and complex configurations is observed. From the perspective of three-dimensional symmetry, these system configurations can be classified into six distinct point groups based on Schönflies notation (Fig. 2a-f). Building on this classification, we construct the corresponding configurational phase diagrams in Fig. 2g,h.

In the following, we provide a detailed analysis of the configuration transitions shown in Fig. 2a-f, which are best understood in conjunction with Fig. 2g,h.

For a filament-free vesicle at $v = 0.9$, equilibrium is reached with an axisymmetric prolate ellipsoid; the maximum radial distance from the axis of revolution to the vesicle surface is $0.738R$. Consequently, when a homogeneous filament loop of length $L \le L_{c1} = 2\pi \times 0.738R = 4.637R$ is present, the filament—regardless of its stiffness—maintains a circular configuration perpendicular to the symmetry axis (Fig. 2a), yielding axisymmetric system configurations ($C_{\infty v}$ symmetry with an infinite number of reflection planes containing the rotation axis).

As the filament length L increases beyond L_{c1}, the filament–vesicle interplay becomes significant, and the confined filament buckles under the distributed compressive forces of the vesicle membrane, driving the system toward non-axisymmetric configurations (Fig. 2b). For highly flexible filaments (e.g., $YI/(\kappa R) = 0.3$ or 1), the vesicle retains its elongated prolate shape, as the filaments exert minimal deformation forces. In this case, the filaments reorient along the available space on the vesicle's long axis, eventually straightening into an oval-like configuration that is predominantly planar yet exhibits modest out-of-plane deviations. In contrast, for relatively stiff filaments (e.g., $YI/(\kappa R) = 10$), the filament reorients but withstands the compressive contact forces from the vesicle to a certain extent, causing pronounced lateral distortion of the vesicle, even leading to an oblate shape. The resulting system configurations in Fig. 2b exhibit C_{2h} symmetry, characterized by a reflection plane and a two-fold axis of rotation. These configurational transitions are summarized in the phase diagrams (Fig. 2g,h).

With further increases in L, the effect of filament stiffness becomes more pronounced, and the system symmetry diverges accordingly (Fig. 2c,e). For relatively flexible filament loops with extended length (e.g., $YI/(\kappa R) = 0.5$ and $L = 7.33R$, Fig. 2c), the oval loops further narrow and reorient into a planar configuration, yielding D_{2h} symmetry, defined by three mutually perpendicular reflection planes intersecting at an inversion center. As the filament length increases further (e.g., $YI/(\kappa R) = 3$ and $L = 9.5R$, Fig. 2d), the lack of additional space for the filament to spread induces supercritical configurational destabilization of the loop, prompting a transition from D_{2h} to D_2 symmetry, characterized with three two-fold rotation axes but lacking reflection planes (left configuration in Fig. 2d). In this state, the filament loop adopts a twisted, figure-eight (or a saddle-like shape, depending on the view direction) within the slightly deformed vesicle.

For stiff filament loops with extended length (e.g., $YI/(\kappa R) = 30$ and $L = 7.5R$, Fig. 2e), the loops resist the compressive forces from the deformed vesicle, enabling radial expansion. The vesicle, in response, flattens while preserving vertical symmetry. The resulting axisymmetric system exhibits $D_{\infty h}$ symmetry, characterized by axial symmetry and an inversion center. The critical length for the shape transition from C_{2h} (Fig. 2b) to $D_{\infty h}$ (Fig. 2e) can be estimated as follows. Recall that a filament-free vesicle at a reduced volume $v = 0.9$, the energy-metastable axisymmetric oblate shape has a maximum radial displacement of the membrane relative to the symmetry axis of $1.162R$, a stiff loop positioned at the equatorial plane of the oblate vesicle will undergo confined radial expansion when its length L exceeds $2\pi \times 1.162R = 7.30R$. This expansion continues until buckling instabilities arise due to vesicle-induced compressive forces (Fig. 2e), accompanied by the system adopting $D_{\infty h}$ symmetry.

As L increases further, intensifying compressive forces cause the filament to bend significantly out of the plane. The loop configuration evolves from a planar circular shape (Fig. 2e) to a saddle shape (Fig. 2f) that exhibits D_{2d} symmetry, defined by two reflection planes containing a two-fold rotation axis. Upon further increases in $YI/(\kappa R)$ and L/R, the loop configuration with more straightened segments becomes energetically favored. To mitigate the energy costs associated with pronounced out-of-plane bending in the saddle shape, the filament adopts a twisted configuration that reduces deformation in two half-loops, driving a system symmetry transition from D_{2d} (e.g., $YI/(\kappa R) = 50$ and $L = 8R$, Fig. 2f) to D_2 symmetry (e.g., $YI/(\kappa R) = 50$ and $L = 9R$, Fig. 2d).

Building on the mapping of all possible system configurations (representative cases in Fig. 2a-f), the corresponding configurational phase diagram is constructed in Fig. 2g. Numerical optimization results indicate that all phase transitions are continuous. A zoom-in view around the D_{2h} region is shown in Fig. 2h. Further numerical analysis indicates that the boundary between phases e and f in Fig. 2g can be roughly approximated by the classical elastic buckling condition for circular rings under uniform pressure (Boresi, 1955), where, in our case, the compressive contact force per unit length exerted by the vesicle confinement acts as the effective pressure.

To elucidate the physical mechanisms underlying these transitions, Fig. 3 displays the profiles of the total elastic energy change $\Delta E_{tot} = \Delta E_m + \Delta E_f$, along with its individual components. The ground energy state consists of a filament-free vesicle at $v = 0.9$ and a circular filament of a length L, so that $\Delta E_m = E_m - 29.9\kappa$ and $\Delta E_f = E_f - 2\pi^2 YI/L$. For $L \le L_{c1}$, the ground state is unperturbed ($\Delta E_{tot} = 0$). As L exceeds L_{c1}, deformation occurs in the filament, the vesicle, or both, with the dominant contribution to ΔE_{tot} determined by their interplay. For the highly flexible filament (e.g., $YI/(\kappa R) = 0.5$ in Fig. 3a), the filament energy change ΔE_f dominates ΔE_{tot} throughout the evolution. In contrast, for stiffer filaments (e.g., $YI/(\kappa R) = 1$ and 30 in Fig. 3b,c), the membrane energy change ΔE_m dominates for intermediate filament lengths, while ΔE_f again becomes dominant at large L/R.

In our system, the vesicle is constrained to have a fixed surface area A and enclosed volume V, which are imposed as equality constraints during energy minimization. These constraints give rise to two Lagrange multipliers: the membrane tension σ and the pressure difference Δp across the vesicle membrane, defined as

$$\sigma = -\left(\frac{\partial E_{tot}}{\partial A}\right)_V \quad \text{and} \quad \Delta p = \left(\frac{\partial E_{tot}}{\partial V}\right)_A,$$

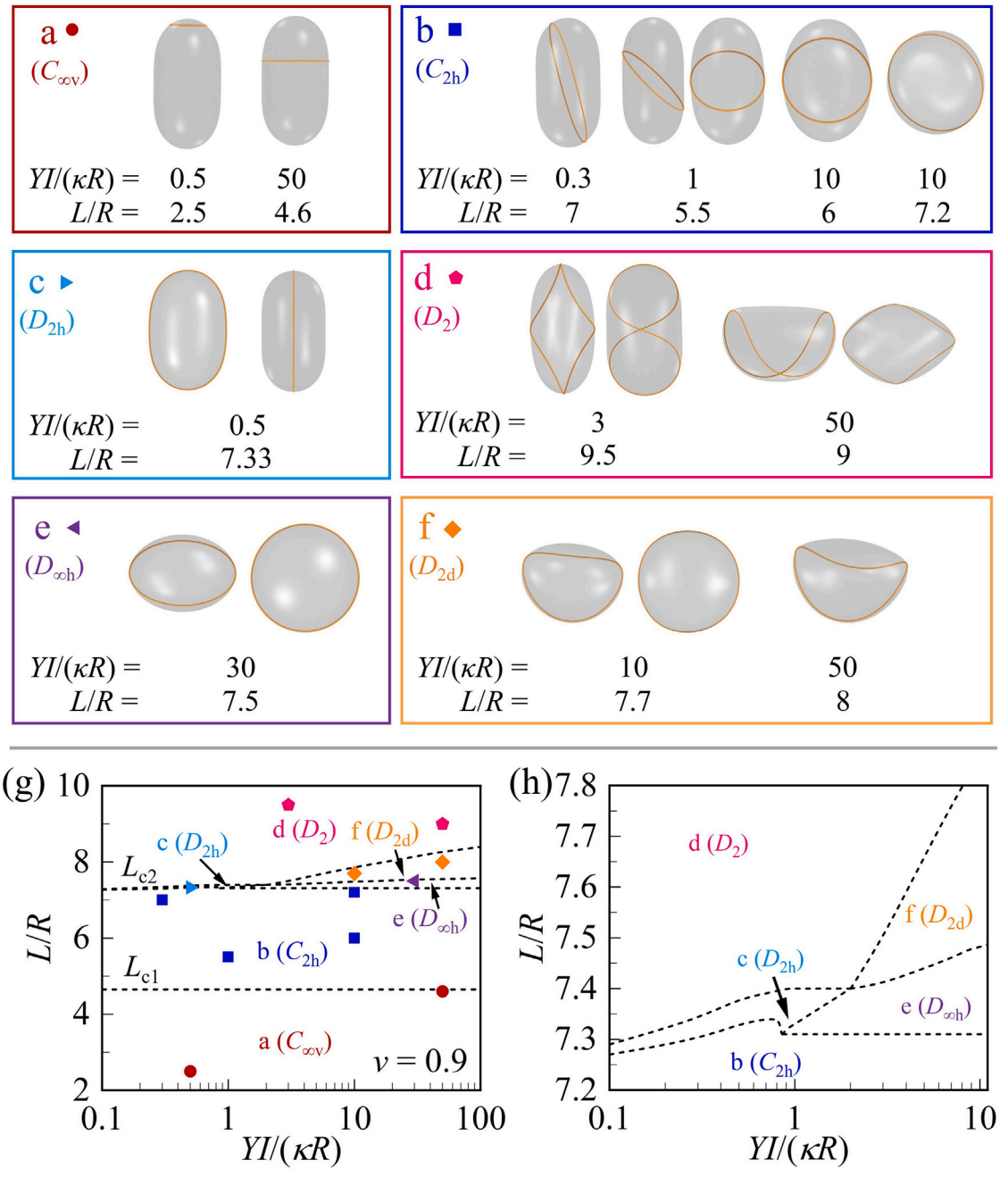

Fig. 2. Representative configurations (a-f) and configurational phase diagrams (g,h) of the closed filament–vesicle system at reduced volume $v = 0.9$ for different values of the relative filament stiffness $YI/(\kappa R)$ and filament length L/R. For clarity, some configurations are presented with views from multiple directions. Six distinct configuration symmetries (a-f) are identified and classified using Schönflies notation, with their respective names indicated in parentheses. Symbols in (g) and (h) correspond to the specific system configurations shown in (a-f). Panel (h) provides a magnified view of a selected region from panel (g). The critical filament length separating phases a and b, and phases b and e, are $L_{c1} = 4.637R$ and L_{c2} slightly larger than $7.30R$, respectively.

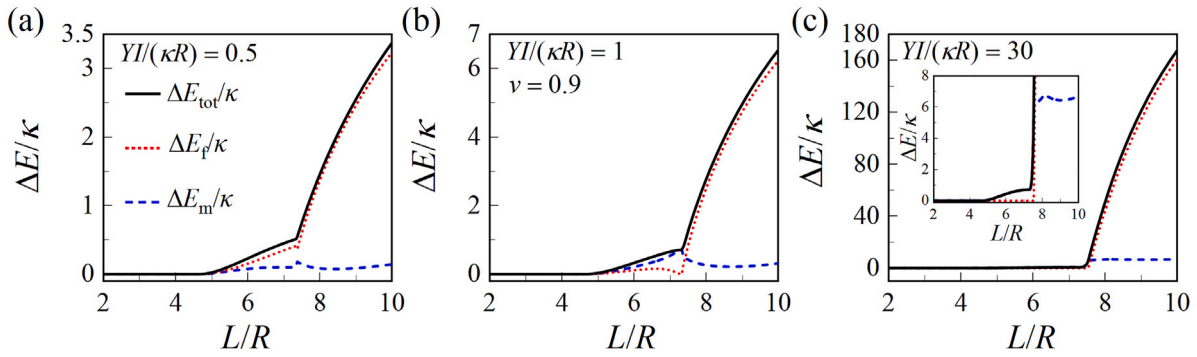

Fig. 3. Profiles of the total elastic energy change ΔE_{tot} and its contributions from the filament ΔE_f and the vesicle membrane ΔE_m for the system at $\upsilon = 0.9$, with $YI/(\kappa R) = 0.5$ (a), 1 (b), and 30 (c). Inset in (c) provides an enlarged view for clarity.

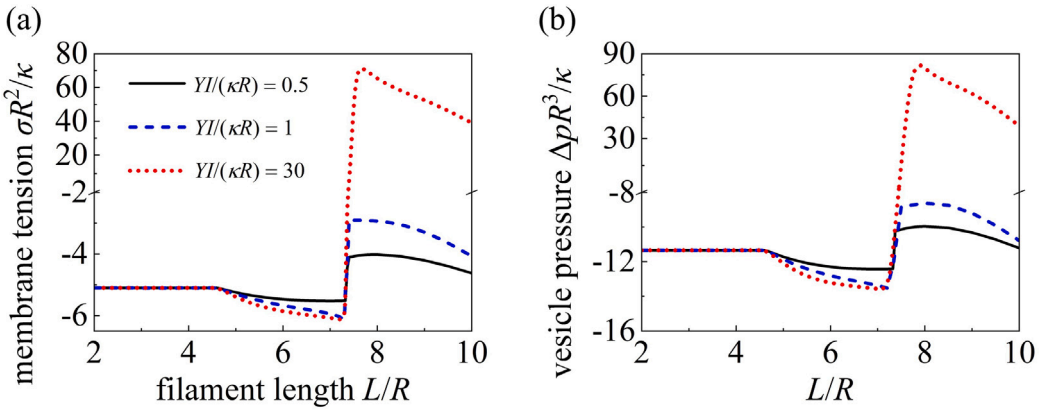

Fig. 4. Membrane tension σ and pressure difference Δp as functions of the normalized filament length L/R at $\upsilon = 0.9$ for $YI/(\kappa R) = 0.5$, 1, and 30. Positive (negative) values of σ indicate tensile (compressive) membrane tension. Positive (negative) values of Δp indicate that the internal pressure of the vesicle is higher (lower) than the external pressure, corresponding to an inflated (deflated) vesicle state.

where the subscripts denote quantities evaluated while holding the other variable constant. A positive σ corresponds to a tensile membrane state, while a positive Δp indicates that the internal pressure exceeds the external pressure, i.e., the vesicle is in an inflated state. These two quantities serve as key mechanical indicators of the system's response to internal filament-induced forces and deformation behavior, offering essential insight into the mechanical stability and morphological transitions of the filament–vesicle systems.

Fig. 4 shows the profiles of membrane tension σ and vesicle pressure difference Δp at $\upsilon = 0.9$. For the flexible filament with $YI/(\kappa R) = 0.5$, a relatively slight but sharp rise in σ from a lower to a larger negative value corresponds to the supercritical buckling of the confined flexible loop (Fig. 4a), occurring through continuous configurational transitions with minor vesicle deformation. For the filaments with $YI/(\kappa R) = 1$ and 30, sharp rises in σ are associated with substantial vesicle shape changes into a flattened configuration. For $L \le L_{c1}$, the system remains in the ground state, exhibiting a compressive membrane tension $\sigma \approx -5.105\kappa/R^2$, identical to that of a filament-free vesicle at $\upsilon = 0.9$. For $YI/(\kappa R) = 0.5$, the prolate vesicle experiences slight deformation as the filament length increases, so that the evolution of σ deviates minimally from the filament-free case, and σ remains compressive. As $YI/(\kappa R)$ increases, the vesicle deformation becomes more pronounced, leading to greater deviations in σ from the filament-free scenario. For the very stiff filament $YI/(\kappa R) = 30$, σ becomes positive at large L/R, indicating that the vesicle undergoes tensile stretching or expansion in the D_2, D_{2d}, and $D_{\infty h}$ configurations.

The variation of pressure difference Δp (Fig. 4b) exhibits a trend similar to that of membrane tension σ (Fig. 4a), reflecting the underlying mechanical balance that governs the vesicle's shape and stress distribution. This consistency is also physically intuitive: for example, an inflated vesicle with positive internal pressure typically exhibits a tensile membrane tension, while a deflated vesicle tends to have negative pressure and compressive tension.

Fig. 5 plots the geometric and force properties of the filament loops at $\upsilon = 0.9$. The torsion T quantifies the deviation of the loop from the osculating plane spanned by the unit tangent vector $\mathbf{t}^f$ and unit normal vector $\mathbf{n}^f$ of the loop. A positive T means that the filament loop bends out-of-plane toward the direction of $\mathbf{t}^f \times \mathbf{b}^f$, and negative when it bends in the opposite direction. At $YI/(\kappa R) = 0.3$ and $L/R = 7$ (Fig. 2b), both its curvature $C(s)$ and torsion $T(s)$ of the filament loop in the C_{2h} configuration exhibit a periodicity of $L/2$. The nonzero geodesic curvature $C_g(s)$ confirms that the filament in Fig. 2b undergoes out-of-plane deformation.

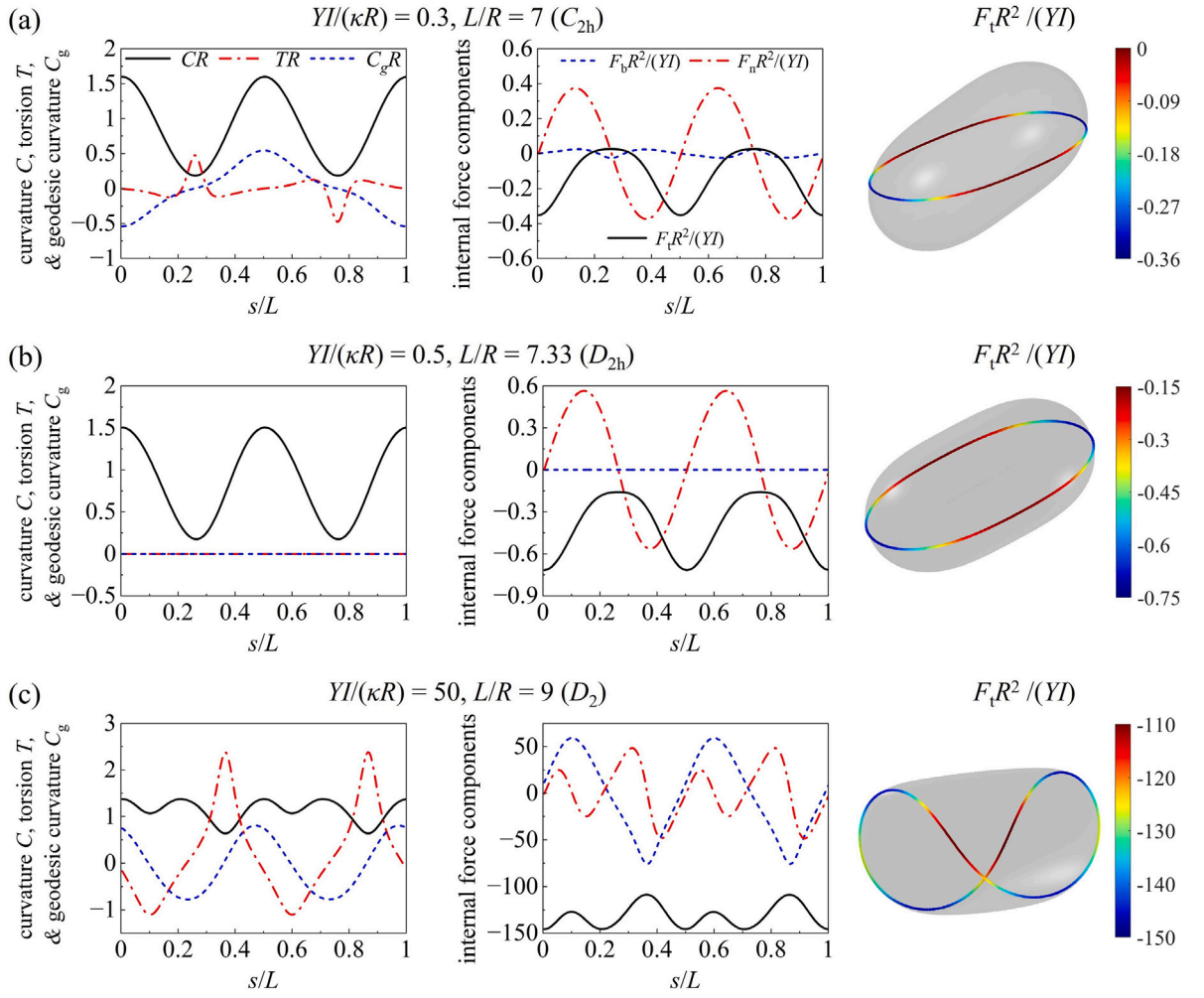

Fig. 5. Geometry and force characteristics of the confined filament loops in vesicles at $v = 0.9$. (a) $YI/(\kappa R) = 0.3$ and $L/R = 7$, (b) $YI/(\kappa R) = 0.5$ and $L/R = 7.33$, and (c) $YI/(\kappa R) = 50$ and $L/R = 9$. A positive (negative) F_t indicates tensile (compressive) tangential internal force. A positive F_n is directed along the positive normal vector $\mathbf{n}^f$, while a positive F_b aligns with the positive binormal vector $\mathbf{b}^f$. The right column shows the distributions of the normalized tangential internal force $F_tR^2/(YI)$ plotted along the arclength.

In contrast, for the filament with $YI/(\kappa R) = 0.5$ and $L/R = 7.33$ (Fig. 2c), the loop exhibits vanishing torsion and positive curvature (Fig. 5b), indicative of a convex, nearly planar configuration. The torsion profiles in Fig. 5 confirm a classical theorem in differential geometry, which states that the torsion of a simple, closed, convex space curve must change sign at least four times (Thorbesson and Umehara, 1999).

Using these geometric details, the filament internal force $\mathbf{F} = F_t\mathbf{t}^f + F_n\mathbf{n}^f + F_b\mathbf{b}^f$ can be determined from Eqs. (4) and (5). For example, the filament shown in the left panel of Fig. 2b bears a compressive tangential internal force ($F_t < 0$) in segments of relatively high curvature, while rest segments with relatively low curvature exhibit a tensile $F_t(> 0)$ (Fig. 5a). The planar filament in Fig. 2c experiences a compressive F_t throughout (Fig. 5b), consistent with the supercritical buckling of the filament. The twisted, figure-eight-shaped long filament in the right panel of Fig. 2d shows a compressive F_t (Fig. 5c) owing to the vesicle confinement.

3.2. The filament–vesicle system at a reduced volume of $v = 0.7$

Compared to the convex surface of a filament-free vesicle at reduced volume $v = 0.9$, the vesicle at $v = 0.7$ adopts a concave dumbbell-like morphology with two spheroidal lobes. How this geometrical difference affects filament packing remains unknown. Here, we explore the filament packing within the vesicle at $v = 0.7$. Representative system configurations for different parameter sets $(L/R, YI/(\kappa R))$ are shown in Fig. 6a-g, classified into six distinct point groups, which form the basis for the configurational phase diagrams in Fig. 6h,i.

The following discussion provides a detailed examination of the configuration transitions depicted in Fig. 6a-g, which are best interpreted in conjunction with Fig. 6h,i.

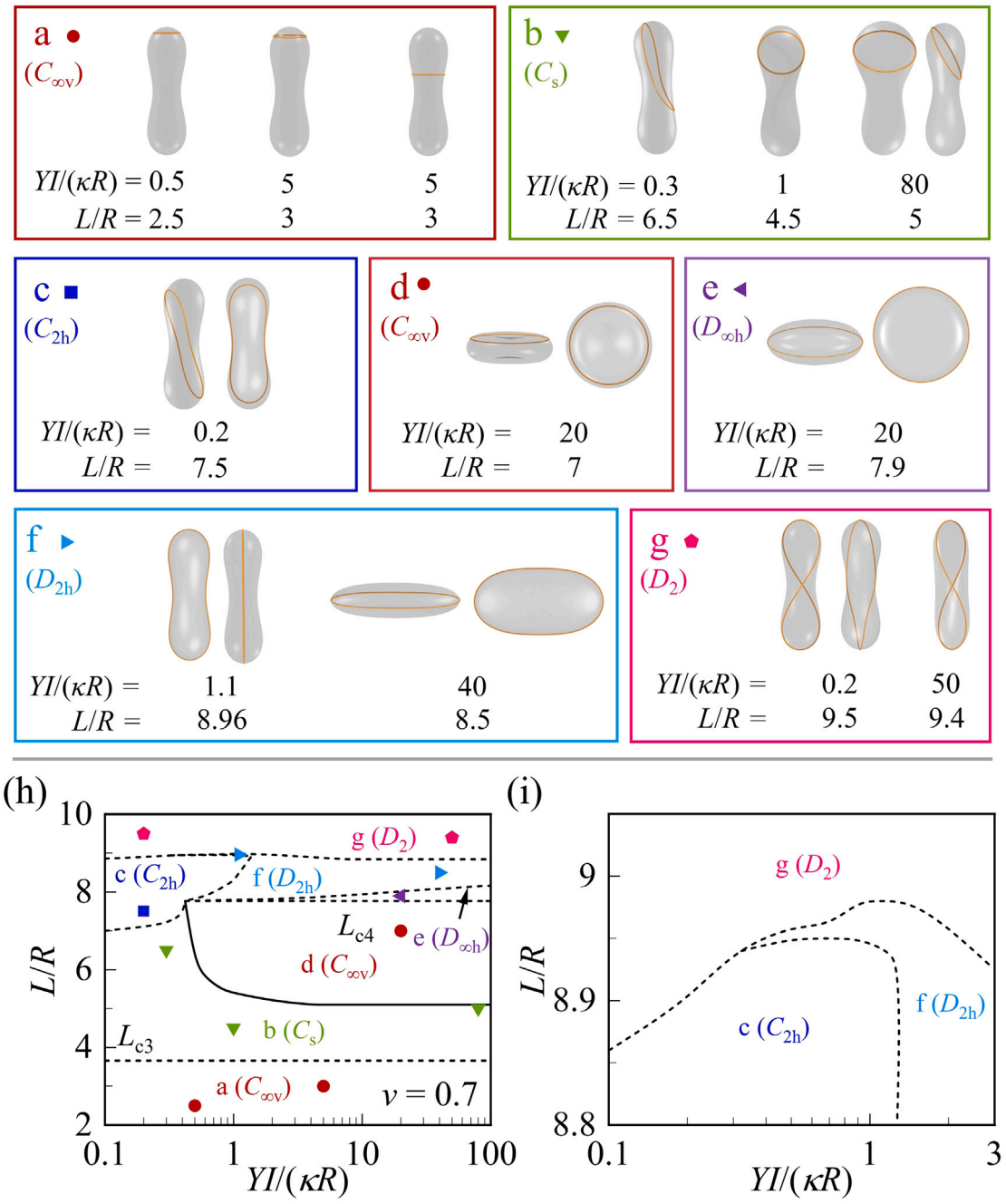

Fig. 6. Representative configurations (a-g) and configurational phase diagrams (h,i) of the closed filament–vesicle system at reduced volume $\upsilon = 0.7$ for various values of $YI/(\kappa R)$ and L/R. To enhance clarity, some configurations are shown from multiple perspectives. Six distinct configurational symmetries (a-g) are identified, with their corresponding symmetry labels indicated in parentheses. Symbols in (h) and (i) denote the specific system configurations shown in (a-g), with panel (i) providing a magnified view of a selected region from (h). The critical filament lengths defining the transitions from phase a to b and from d to e are $L_{c3} = 3.64R$ and $L_{c4} = 7.72R$, respectively.

For a free vesicle of a prolate dumbbell shape at $\upsilon = 0.7$, the maximum radial distance from the axis of revolution to the vesicle surface is $0.58R$. As a result, when a homogeneous filament loop of length $L \le L_{c3} = 2\pi \times 0.58R = 3.64R$ is introduced, it remains circular and oriented perpendicular to the symmetry axis, irrespective of its bending stiffness (Fig. 6a). This configuration preserves the system's axial symmetry, corresponding to the $C_{\infty v}$ symmetry group.

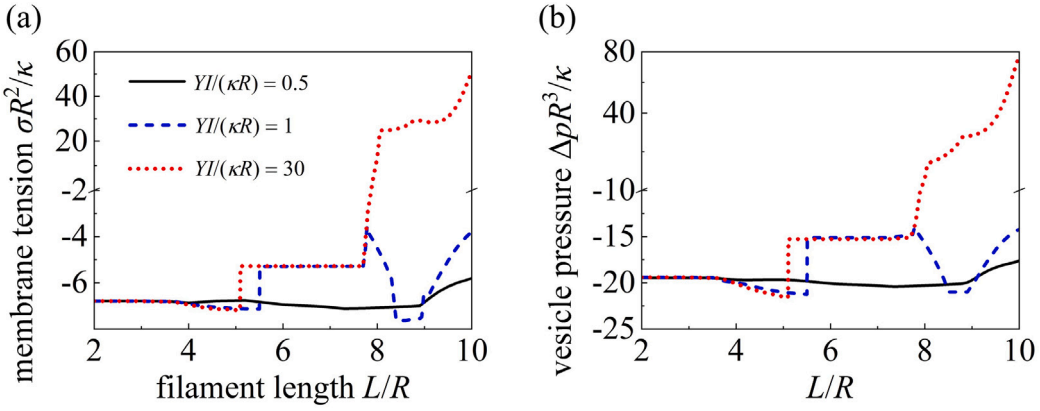

Fig. 7. Membrane tension σ and pressure difference Δp as functions of the normalized filament length L/R at $\upsilon = 0.7$ for relative filament stiffness values $YI/(\kappa R) = 0.5$, 1, and 30. Positive σ indicates tensile membrane tension, while negative σ corresponds to compressive membrane tension. Positive Δp indicates an inflated vesicle state, while negative Δp corresponds to a deflated vesicle state.

As the filament length L increases beyond L_{c3}, the vesicle lobes accommodate the filament loop with minor deformation (left panel of Fig. 6b). For a highly flexible loop with longer length, the filament barely deforms the vesicle lobe, instead narrowing and elongating into the vesicle's waist and even the opposing lobe (middle panel of Fig. 6b). In contrast, a stiff loop of comparable length significantly deforms and expands its resident lobe (right panel of Fig. 6b). These configurations exhibit C_s symmetry with a single reflection plane.

For the very flexible loops, further increasing L drives the filament to distribute equally between the two lobes of the dumbbell vesicle, resulting in a configuration with C_{2h} symmetry (Fig. 6c). Note that the filament in this state does not generally adopt a planar configuration.

For moderately stiff to stiff filaments with relatively long L (Fig. 6d), the loops embedded within the vesicle lobe expand robustly, counteracting compressive stresses exerted by the vesicle membrane. This mechanical resistance drives a morphological transition from a prolate, dumbbell-shaped vesicle to an oblate configuration, resulting in a system with $C_{\infty v}$ symmetry. Notably, for a filament-free vesicle at reduced volume $\upsilon = 0.7$, the axisymmetric oblate shape corresponds to an energy-metastable state, where the maximum radial displacement of the membrane relative to the symmetry axis is $1.229R$. Consequently, stiff loops in configurations such as those shown in Fig. 6d, with lengths $L \le L_{c4} = 2\pi \times 1.229R = 7.72R$, maintain their initial circular geometry perpendicular to the symmetry axis. It is worth noting that when L is just below L_{c4}, an alternative configuration may appear during optimization: an oblate vesicle with a slightly inclined and weakly deformed filament loop, which possesses a marginally higher system energy.

When L exceeds L_{c4}, the stiff loop—now positioned at the vesicle's equatorial plane—undergoes continued expansion until buckling instabilities arise due to the distributed compressive force exerted by the vesicle (Fig. 6e). Accompanying this radial expansion, the system adopts $D_{\infty h}$ symmetry. In this configuration, the vesicle may exhibit either a convex or concave morphology.

For even longer filaments (e.g., $YI/(\kappa R) = 40$, $L = 8.5R$, Fig. 6f), increasing compressive contact forces induce supercritical buckling, leading the filament loop to adopt an oval configuration. This results in a symmetry transition from $D_{\infty h}$ to D_{2h}.

At even greater filament lengths (Fig. 6g), spatial constraints prevent further in-plane expansion of both flexible and stiff loops, leading to significant out-of-plane bending. This results in a twisted, figure-eight or saddle-like configuration, depending on the viewing direction, characterized by D_2 symmetry.

Following systematic enumeration of accessible morphological states (representative cases in Fig. 6a-g), we establish the configurational phase diagram in Fig. 6h, with the dashed curves representing the continuous configurational transitions and the solid line denoting the discontinuous transition. Fig. 6i highlights the tri-critical region near the C_{2h}-D_2-D_{2h} symmetry intersection.

Taking the ground energy state as a free vesicle at $\upsilon = 0.7$ and a circular filament of length L, the energy changes are $\Delta E_m = E_m - 41.3\kappa$ and $\Delta E_f = E_f - 2\pi^2 YI/L$. For $L \le L_{c3}$, the system remains in its unperturbed ground state ($\Delta E_{tot} = 0$). As L exceeds L_{c3}, the dominant contribution to ΔE_{tot} is determined by the filament–vesicle interplay (Fig. S1). Similar to the case of $\upsilon = 0.9$, for highly flexible filaments, ΔE_f dominates ΔE_{tot} throughout the evolution. In contrast, for stiffer filaments, ΔE_m dominates at intermediate L/R, while ΔE_f regains dominance at large L/R.

Fig. 7 shows the membrane tension profiles at $\upsilon = 0.7$ for different filament stiffness values. For $L \le L_{c3}$, the system is in the ground state, exhibiting compressive $\sigma \approx -6.788\kappa/R^2$, identical to that of a filament-free dumbbell-shaped vesicle at $\upsilon = 0.7$. At $L = L_{c4}$, $\sigma \approx -5.288\kappa/R^2$ corresponds to the oblate vesicle configuration. For the filaments with $YI/(\kappa R) = 1$ and 30, two sharp rises in σ are observed, signaling substantial vesicle shape changes into an oblate and subsequently into a more flattened configuration. The geometry and force characteristics of selected filament loops in Fig. 6c, right panel of Fig. 6f, and left panel of Fig. 6g are shown in Fig. S2. The pressure difference Δp shows a variation pattern that parallels that of membrane tension σ, consistent with the overall mechanical balance of the vesicle system.

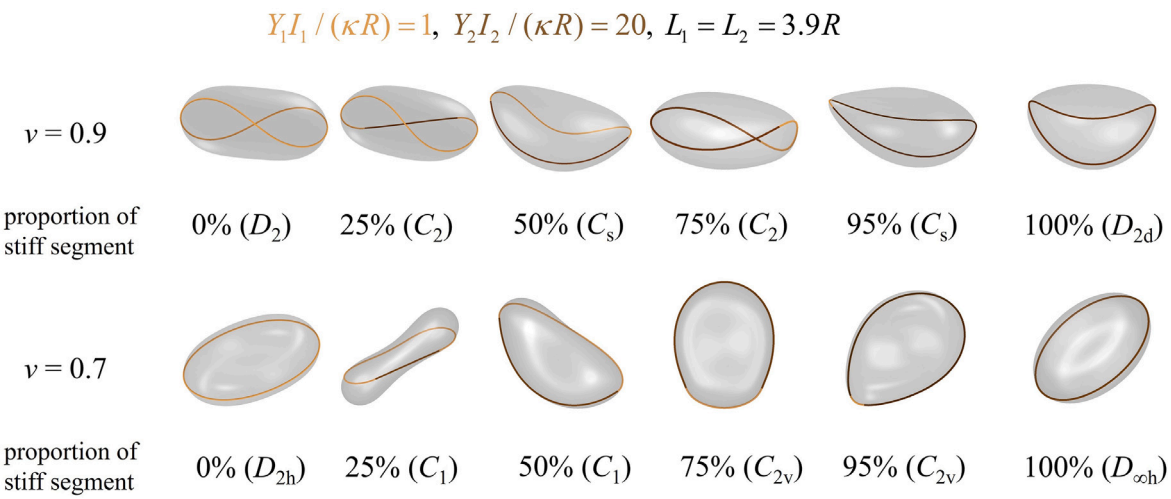

Fig. 8. Selected system configurations with inhomogeneous filaments at reduced vesicle volume $v = 0.9$ and 0.7. The configurational symmetry groups are shown on the right side of the stiff segment proportion. Each inhomogeneous filament has two segments, more flexible segment #1 (light yellow) of length L_1 and bending stiffness Y_1I_1, and stiffer segment #2 (dark brown) of length L_2 and bending stiffness Y_2I_2. Here $Y_1I_1/(\kappa R) = 1$, $Y_2I_2/(\kappa R) = 20$, and $L_1 = L_2 = 3.9R$ are taken.

4. Vesicular packing of inhomogeneous filament loops

Cellular filaments can exhibit localized mechanical heterogeneity due to protein-specific interactions (Blanchoin et al., 2014). For example, cofilin-decorated actin filaments display enhanced flexibility and fragmentation susceptibility (McCullough et al., 2008), while tropomyosin-troponin complexes stabilize actin filaments to increase rigidity (Goldmann, 2000). To investigate how such filament inhomogeneity governs system morphologies, we simulate inhomogeneous filaments—comprising alternating flexible and stiff segments—confined within vesicles at reduced volumes $v = 0.9$ and 0.7. By systematically varying the stiff segment's length proportion, we observe striking morphological transitions (Fig. 8). Supplementary energy and membrane tension profiles for the system are shown in Fig. S3.

For the cases in the top panel of Fig. 8 at $v = 0.9$, increasing the stiff segment proportion transforms the system from a convex prolate vesicle with a twisted, flexible filament loop to a pebble-shaped vesicle containing a saddle-shaped stiff filament. Similarly, at $v = 0.7$, a concave dumbbell-shaped vesicle with an elongated flexible loop evolves into a flattened configuration with a circular stiff loop (Fig. 8, bottom panel). In cases of around 50% stiff segments, one can observe that the bending deformation localizes primarily at two ends of the flexible segment, effectively minimizing the bending energy cost. Moreover, by introducing a very short flexible segment (e.g., 5% flexible and 95% stiff), filament bending in kinks can be captured.

5. Discussion

The rich morphologies observed in our system arise from the interplay between two primary factors: the anisotropic nature of the confining geometry and the mechanical coupling between filaments and vesicles. The first factor, geometric anisotropy, acts as a potent driver of symmetry breaking. Transitioning from isotropic to anisotropic confinement fundamentally alters the filament's accessible configuration space and reshapes the underlying energy landscape. In spherical confinements, the conformational ensemble is governed by continuous rotational symmetry, suppressing the emergence of lower-symmetry states and favoring highly symmetric states with D_{2d} symmetry (Vázquez-Montejo et al., 2015; Wang et al., 2024), which occupy broad regions of the morphological phase space. In contrast, anisotropic boundaries such as prolate, oblate, or cylindrical shapes break this symmetry and introduce directional energetic biases that favor filament alignment along specific directions of the confinement. Closed filament loops are subject to topological constraints that enforce global coupling along their contour. As a result, local alignment preferences must reconcile with the cooperative deformation of filament segments residing in regions with differing curvature. This global compromise amplifies geometric frustration and often leads to complex filament configurations with reduced symmetry. Our simulations directly capture this effect: compared to relatively rounded vesicles exhibiting D_{2d} symmetry (Fig. 2f), elongated vesicle shapes frequently give rise to filament organizations with lower degrees of symmetry, including C_s (Fig. 6b), C_{2h} (Figs. 2b and 6c), and D_2 (Figs. 2d and 6g), with D_{2h} (Figs. 2c and 6f) representing a special case of comparable symmetry to D_{2d}.

The second factor is the bidirectional interaction between the filament and vesicle. As the filament extends, buckles, or reorients, it exerts localized and distributed forces on the enclosing membrane, inducing shape changes such as flattening, elongation, or expanded lobe formation. In turn, the vesicle responds by reshaping its geometry to minimize elastic energy under fixed area and

volume constraints. This deformation feeds back onto the filament, modifying the local confinement landscape and thus constraining the filament's accessible configurations. Unlike rigid confinements, where the filament adapts passively to a prescribed boundary, the deformable vesicle enables a soft, responsive confinement, in which filament and membrane coevolve toward energetically favorable morphologies through a trade-off between filament bending resistance and membrane curvature elasticity. Our simulations illustrate this mutual interaction clearly: the system's morphological transitions result from a delicate balance between filament bending resistance and membrane elasticity. Importantly, this mechanical coupling enables configurational transformations within the system without artificially altering the imposed boundary morphology. Viewed in the context of system evolution, these transitions underscore the role of mechanical coupling as a dynamic organizing mechanism for symmetry breaking, energy redistribution, and morphological diversity in the filament–vesicle systems.

The interplay between geometric anisotropy and mechanical coupling helps explain key differences between the phase diagrams observed under fixed volume (Figs. 2 and 6) and those under zero osmotic pressure, where the vesicle is free to adjust its volume (Shi et al., 2023). Under the latter condition, depending on $(L/R, YI/(\kappa R))$, the confined filament loops adopt a variety of shapes, including circles (associated with $D_{\infty h}$ system symmetries), ovals (D_{2h}), saddles (C_{2v}), and twisted figure-eight forms (D_2) (Shi et al., 2023). In comparison with the phase diagrams in Figs. 2 and 6, several morphologies identified here with lower symmetries, such as C_{2h}, D_{2d}, and C_s, are absent at zero osmotic pressure. This difference reflects the nature of the confinement: at fixed reduced volume, the nonspherical vesicle shapes introduce intrinsic anisotropy, favoring lower-symmetry filament configurations adapted to geometric asymmetry. By contrast, at zero osmotic pressure, the isotropic spherical vesicle confinement does not favor biased directional filament buckling or asymmetry, thereby instead stabilizing higher-symmetry filament configurations.

The predicted morphologies of the closed filament–vesicle system—including circular, oval, saddle, and figure-eight-shaped loops (Figs. 2 and 6)—closely resemble structures observed in various cellular contexts. These include actin polymerization in vesicles, where filament length and stiffness are regulated through changes in Mg^{2+} concentration, temperature (Limozin and Sackmann, 2002), and fascin-to-actin molar ratio (Tsai and Koenderink, 2015). Similar morphological transitions are observed during the discoid-to-spherical transformation of platelets upon activation, where the microtubule-based marginal band shifts from a circular or oval loop to saddle-shaped configurations (Diagouraga et al., 2014). This transition is attributed to an increase in the relative filament length within the confined environment. An additional comparison arises from the packing of DNA in highly elongated bacteriophages, where the confined genome adopts a twisted, figure-eight-like structure (Petrov et al., 2007), analogous to our predictions for long, relatively flexible filaments enclosed within elongated vesicles (Figs. 2d and 6g).

A close inspection of the configurational phase diagrams at reduced volumes $v = 0.9$ and $v = 0.7$ exhibit two notable structural differences (Figs. 2 and 6). At $v = 0.9$, a C_{2h}-symmetric phase appears (Fig. 2), whereas at $v = 0.7$, this phase is replaced by a combination of C_s and $C_{\infty v}$-symmetric phases (Fig. 6). This distinction arises from the intrinsic differences in vesicle geometry. At $v = 0.7$, the filament-free vesicle adopts a dumbbell-like shape characterized by a pronounced waist constriction that effectively divides the vesicle into two spheroidal lobes. By contrast, at $v = 0.9$, the vesicle retains a uniformly elongated, barrel-like shape without such narrowing. At $v = 0.9$, the filament (Fig. 2b) can readily span the vesicle's midsection, gradually deforming the vesicle from a prolate to an oblate shape as L/R and $YI/(\kappa R)$ increase. In contrast, at $v = 0.7$, the filament loop (Fig. 6b) becomes confined within one lobe of the narrow-waisted prolate dumbbell, as crossing the waist is energetically unfavorable. With increasing filament length, the vesicle undergoes a discontinuous transition from a narrow-waisted prolate with one expanded lobe to an oblate shape (Fig. 6d).

Another difference lies in the absence of the D_{2d}-symmetric phase with the saddle-shaped loops at $v = 0.7$ (Fig. 6). This phase, present at $v = 0.9$ (Fig. 2), requires a vesicle with a relatively widened midsection to accommodate the spatial demands of the loop morphology—conditions that are incompatible with the strongly constricted shapes at a lower volume $v = 0.7$.

The phase behaviors in Figs. 2 and 6, along with their marked differences, highlight that tuning filament length and stiffness provides an effective mechanism for controlling vesicle morphology. Experimentally, such regulation could be achieved by promoting actin polymerization or actomyosin contraction to control filament length, and by introducing actin bundlers such as talin or vinculin to modulate filament stiffness (Litschel et al., 2021).

In addition to boundary confinement and filament–vesicle coupling, inter- and intra-filament interactions, such as self-repulsion, also play important roles in structural organization. Katzav et al. (2006) proposed a statistical framework for elastic rods confined to spherical surfaces, showing that self-avoidance contributes to a continuous transition from isotropic to nematic order as the sphere radius decreases. Building on this, Grossman and co-workers (Grossman et al., 2021; Grossman and Katzav, 2024) investigated the packing of stiff rods in ellipsoidal geometries and demonstrated that strong self-avoidance significantly affects packing orientation—inducing a first-order transition from azimuthal to polar alignment in oblate spheroids and generating a deep equatorial metastable state in prolate spheroids.

6. Conclusion

We have theoretically investigated the morphogenesis of the filament–vesicle system with different reduced volumes. Modeling the enclosed filament as a surface-constrained thin elastic loop and minimizing the system energy, we uncover a rich array of coupled filament–vesicle morphologies. These include in-plane and out-of-plane filament buckling, filament reorientation, and prolate-to-oblate vesicle shape transitions. The filament adopts a variety of configurations—circular, oval, saddle, and figure-eight—depending on its relative length and stiffness.

The morphological phase diagrams show that a prolate vesicle can be driven into an oblate shape by a filament loop of sufficiently large length and stiffness, with further filament elongation inducing pronounced out-of-plane filament deformation. The underlying shape transition mechanisms are evaluated through energy and membrane tension analyses. For inhomogeneous filament loops, we show that increasing the proportion of stiff segments induces distinct vesicle shape transformations, such as from convex prolate to pebble-shaped vesicles or from elongated to flattened configurations, contingent on the reduced volume. A conceptually driven perspective on the geometric–mechanical feedback reveals how confinement-induced constraints, together with the bidirectional interaction between the filament and vesicle, jointly shape emergent morphologies.

Our findings deepen the understanding of cell shaping and the physical principles governing filament organization in confined cellular environments. They may also guide the design of shape-adaptive synthetic systems, such as artificial cells or programmable structures based on filament–vesicle assemblies. Furthermore, our results provide a foundation for future studies incorporating vesicle spontaneous curvature, filament interaction, filament network reorganization from a topological perspective, and complex mechanical responses of the filament–vesicle system.

CRediT authorship contribution statement

Chao Shi: Writing – original draft, Investigation, Formal analysis. **Chengyao Zhang:** Writing – original draft, Investigation, Formal analysis. **Yaxin Fang:** Investigation. **Xin Yi:** Writing – review & editing, Investigation, Funding acquisition, Formal analysis, Conceptualization.

Declaration of competing interest

The authors declare that they have no known competing financial interests or personal relationships that could have appeared to influence the work reported in this paper.

Acknowledgments

This work was supported by the National Natural Science Foundation of China under Grant No. 12272004. Computation resources supported by the High-performance Computing Platform of Peking University are acknowledged.

Appendix A. Supplementary data

Supplementary material related to this article can be found online at https://doi.org/10.1016/j.jmps.2025.106383.

Data availability

Data will be made available on request.

References

Alves, C.J., et al., 2025. Invasion of glioma cells through confined space requires membrane tension regulation and mechano-electrical coupling via Plexin-B2. Nat. Commun. 16, 272.
Bahrami, A.H., Lin, M.G., Ren, X., Hurley, J.H., Hummer, G., 2017. Scaffolding the cup-shaped double membrane in autophagy. PLoS Comput. Biol. 13, e1005817.
Bashirzadeh, Y., Redford, S.A., Lorpaiboon, C., Groaz, A., Moghimianavval, H., Litschel, T., Schwille, P., Hocky, G.M., Dinner, A.R., Liu, A.P., 2021. Actin crosslinker competition and sorting drive emergent GUV size-dependent actin network architecture. Commun. Biol. 4, 1136.
Behera, A., Kumar, G., Sain, A., 2020. Confined filaments in soft vesicles – the case of sickle red blood cells. Soft Matter 16, 421–427.
Blanchoin, L., Boujemaa-Paterski, R., Sykes, C., Plastino, J., 2014. Actin dynamics, architecture, and mechanics in cell motility. Physiol. Rev. 94, 235–263.
Boresi, A.P., 1955. A refinement of the theory of buckling of rings under uniform pressure. J. Appl. Mech. 22, 95–102.
Bray, D., 2000. Cell Movements: From Molecules To Motility, second ed. Garland Science, New York, United States.
Diagouraga, B., Grichine, A., Fertin, A., Wang, J., Khochbin, S., Sadoul, K., 2014. Motor-driven marginal band coiling promotes cell shape change during platelet activation. J. Cell. Biol. 204, 177–185.
Dmitrieff, S., Alsina, A., Mathur, A., Nédélec, F.J., 2017. Balance of microtubule stiffness and cortical tension determines the size of blood cells with marginal band across species. Proc. Natl. Acad. Sci. USA 114, 4418–4423.
Doi, M., Edwards, S.F., 1986. The Theory of Polymer Dynamics. Oxford University Press, Oxford, United Kingdom.
Filla, N., Gu, B., Hou, J., Song, K., Li, H., Liu, N., Wang, X., 2024. Hyperelasticity of blood clots: Bridging the gap between microscopic and continuum scales. J. Mech. Phys. Solids 190, 105750.
Fletcher, R., 1987. Practical Methods of Optimization, second ed. John Wiley & Sons, Ltd., Chichester, United Kingdom.
Fygenson, D.K., Marko, J.F., Libchaber, A., 1997. Mechanics of microtubule-based membrane extension. Phys. Rev. Lett. 79, 4497–4500.
Ganichkina, O.M., Vancraenenbroeck, R., Rosenblum, G., Hofmann, H., Mikhailov, A.S., Daumke, O., Noel, J.K., 2021. Quantification and demonstration of the collective constriction-by-ratchet mechanism in the dynamin molecular motor. Proc. Natl. Acad. Sci. USA 118, e2101144118.
Goldmann, W.H., 2000. Binding of tropomyosin-troponin to actin increases filament bending stiffness. Biochem. Biophys. Res. Commun. 276, 1225–1228.
Grossman, D., Katzav, E., 2024. Effects of self-avoidance on the packing of stiff rods on ellipsoids. Phys. Rev. E 109, 054111.
Grossman, D., Katzav, E., Sharon, E., 2021. Packing of stiff rods on ellipsoids: Geometry. Phys. Rev. E 103, 013001.
Gu, B., Hou, J., Filla, N., Li, H., Wang, X., 2025. Rupture mechanics of blood clot fibrin fibers: A coarse-grained model study. J. Mech. Phys. Solids 196, 105998.
Guven, J., Vázquez-Montejo, P., 2012. Confinement of semiflexible polymers. Phys. Rev. E 85, 026603.

Helfrich, W., 1973. Elastic properties of lipid bilayers: Theory and possible experiments. Z. Naturforsch. C 28, 693–703.
Katzav, E., Adda-Bedia, M., Boudaoud, A., 2006. A statistical approach to close packing of elastic rods and to DNA packaging in viral capsids. Proc. Natl. Acad. Sci. USA 103, 18900–18904.
Khairy, K., Howard, J., 2011. Minimum-energy vesicle and cell shapes calculated using spherical harmonics parameterization. Soft Matter 7, 2138–2143.
Kreyszig, E., 1991. Differential Geometry. Dover Publications, New York, United States.
Limozin, L., Sackmann, E., 2002. Polymorphism of cross-linked actin networks in giant vesicles. Phys. Rev. Lett. 89, 168103.
Litschel, T., Kelley, C.F., Holz, D., Koudehi, M.A., Vogel, S.K., Burdawan, L., Mizuno, N., Vavylonis, D., Schwille, P., 2021. Reconstitution of contractile actomyosin rings in vesicles. Nat. Commun. 12, 2254.
McCullough, B.R., Blanchoin, L., Martiel, J.-L., De La Cruz, E.M., 2008. Cofilin increases the bending flexibility of actin filaments: Implications for severing and cell mechanics. J. Mol. Biol. 381, 550–558.
McDargh, Z.A., Vázquez-Montejo, P., Guven, J., Deserno, M., 2016. Constriction by dynamin: Elasticity versus adhesion. Biophys. J. 111, 2470–2480.
Meadowcroft, B., Palaja, I., Pfitzner, A.-K., Roux, A., Baum, B., Šarić, A., 2022. Mechanochemical rules for shape-shifting filaments that remodel membranes. Phys. Rev. Lett. 129, 268101.
Miyazaki, M., Chiba, M., Eguchi, H., Ohki, T., Ishiwata, S., 2015. Cell-sized spherical confinement induces the spontaneous formation of contractile actomyosin rings *in vitro*. Nat. Cell Biol. 17, 480–489.
Petrov, A.S., Boz, M.B., Harvey, S.C., 2007. The conformation of double-stranded DNA inside bacteriophages depends on capsid size and shape. J. Struct. Biol. 160, 241–248.
Seifert, U., Berndl, K., Lipowsky, R., 1991. Shape transformations of vesicles: phase diagram for spontaneous-curvature and bilayer-coupling models. Phys. Rev. A 44, 1182–1202.
Sharma, B.L., Perotti, L.E., Dharmavaram, S., 2023. Computational modeling of coupled interactions of fluid membranes with embedded filaments. Comput. Methods Appl. Mech. Engrg. 417, 116441.
Shi, C., Zou, G., Wu, Z., Wang, M., Zhang, X., Gao, H., Yi, X., 2023. Morphological transformations of vesicles with confined flexible filaments. Proc. Natl. Acad. Sci. USA 120, e2300380120.
Szwedziak, P., Wang, Q., Bharat, T.A.M., Tsim, M., Löwe, J., 2014. Architecture of the ring formed by the tubulin homologue FtsZ in bacterial cell division. eLife 3, e04601.
Thorbesson, G., Umehara, M., 1999. A Unified Approach to the Four Vertex Theorems. II, Differential and Symplectic Topology of Knots and Curves. In: Amer. Math. Soc. Transl. Ser. 2. vol. 190, Amer. Math. Soc., Providence, RI, pp. 229–252.
Tortora, M.M.C., Jost, D., 2023. Orientational wetting and topological transitions in confined solutions of semiflexible polymers. Macromolecules 56, 1339–1351.
Tsai, F.-C., Koenderink, G.H., 2015. Shape control of lipid bilayer membranes by confined actin bundles. Soft Matter 11, 8834–8847.
Vázquez-Montejo, P., Božič, B., Guven, J., 2025. Equatorial deformation of homogeneous spherical fluid vesicles by a rigid ring. Phys. Rev. E 111, 035411.
Vázquez-Montejo, P., McDargh, Z., Deserno, M., Guven, J., 2015. Cylindrical confinement of semiflexible polymers. Phys. Rev. E 91, 063203.
Vetter, R., Wittel, F.K., Herrmann, H.J., 2014. Morphogenesis of filaments growing in flexible confinements. Nat. Commun. 5, 4437.
Wang, M., Li, X., Yi, X., 2024. Deformation, shape transformations, and stability of elastic rod loops within spherical confinement. J. Mech. Phys. Solids 191, 105771.
Wang, M., Yi, X., 2024. Equilibrium analysis of surface-constrained elastic rods: Unveiling contact and internal forces through local geometry. J. Mech. Phys. Solids 187, 105635.
Wu, Z., Yuan, H., Zhang, X., Yi, X., 2019. Sidewall contact regulating the nanorod packing inside vesicles with relative volumes. Soft Matter 15, 2552–2559.
Yam, C., He, Y., Zhang, D., Chiang, K.-H., Oliferenko, S., 2011. Divergent strategies for controlling the nuclear membrane satisfy geometric constraints during nuclear division. Curr. Biol. 21, 1314–1319.
Zhang, C., Fang, Y., Shi, C., Yuan, H., Yi, X., 2024. Stretching transition of vesicles with confined filament loops: Morphological evolution with filament distortion and reorientation. Giant 17, 100233.
Zou, G., Yi, X., Zhu, W., Gao, H., 2018. Packing of flexible nanofibers in vesicles. Extreme Mech. Lett. 19, 20–26.

Supporting Information for

Flexible filaments in vesicles with reduced volume: Anisotropic confinement and morphological response

Chao Shi†, Chengyao Zhang†, Yaxin Fang, Xin Yi*

School of Mechanics and Engineering Science, Peking University, Beijing 100871, China

*E-mail: xyi@pku.edu.cn

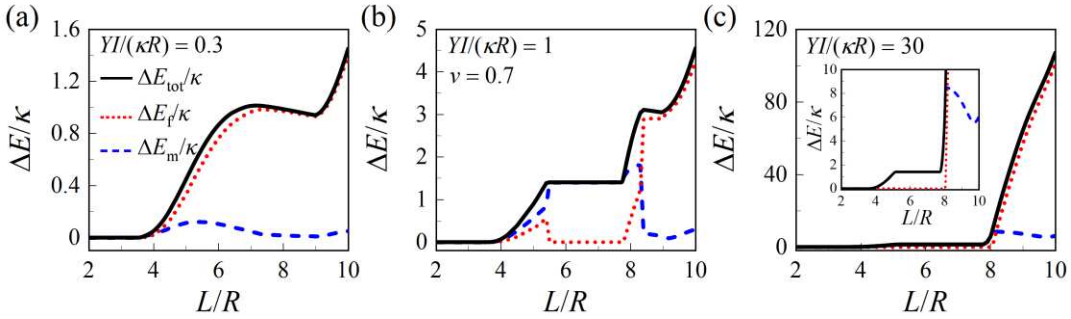

Fig. S1. Profiles of the total elastic energy change ΔE_{tot} and its components ΔE_f and ΔE_m for the system at $v = 0.7$, with $YI/(\kappa R) = 0.3$ (a), 1 (b), and 30 (c). Inset in (c) provides an enlarged view.

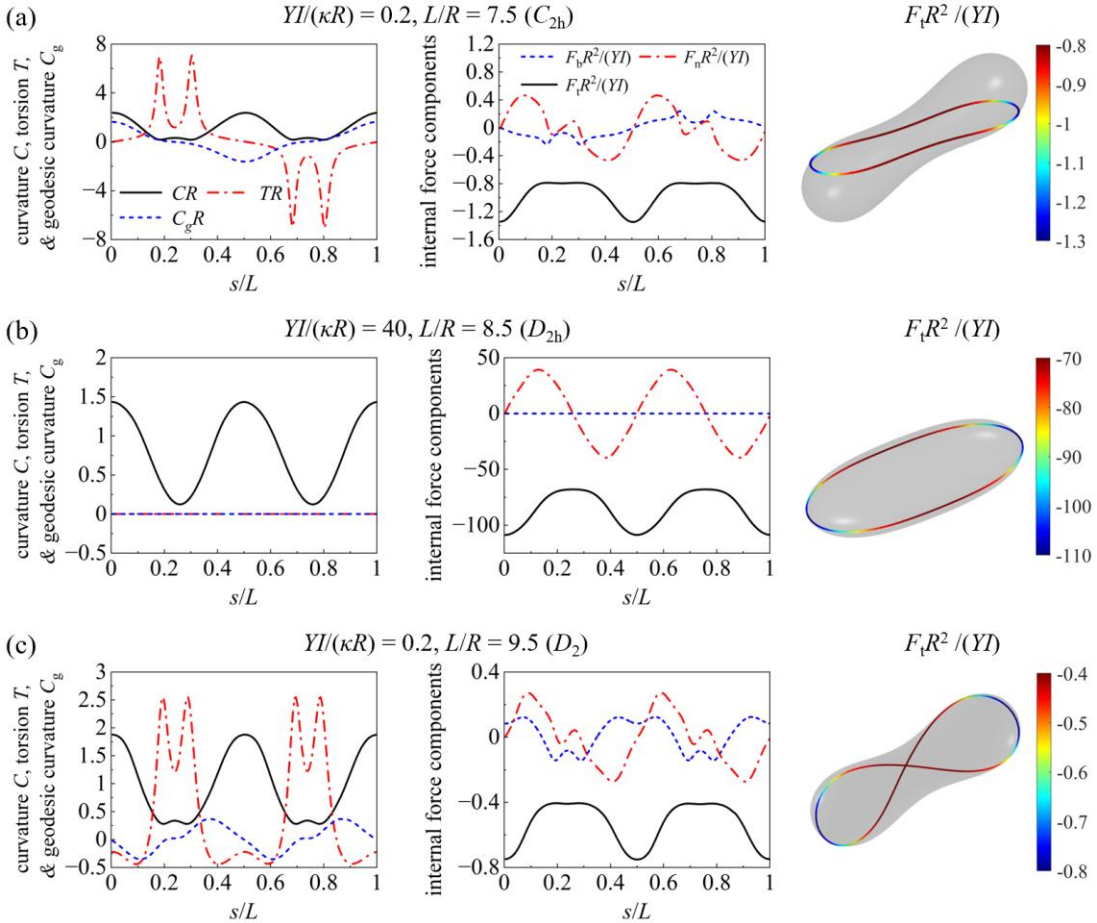

Fig. S2. Geometry and force characteristics of the confined filament loops in vesicles at $v = 0.7$. (a) $YI/(\kappa R) = 0.2$ and $L/R = 7.5$, (b) $YI/(\kappa R) = 40$ and $L/R = 8.5$, and (c) $YI/(\kappa R) = 0.2$ and $L/R = 9.5$. A positive (negative) F_t indicates tensile (compressive) tangential force. A positive F_n is directed along the positive normal vector $\mathbf{n}^f$, while a positive F_b aligns with the positive binormal vector $\mathbf{b}^f$.

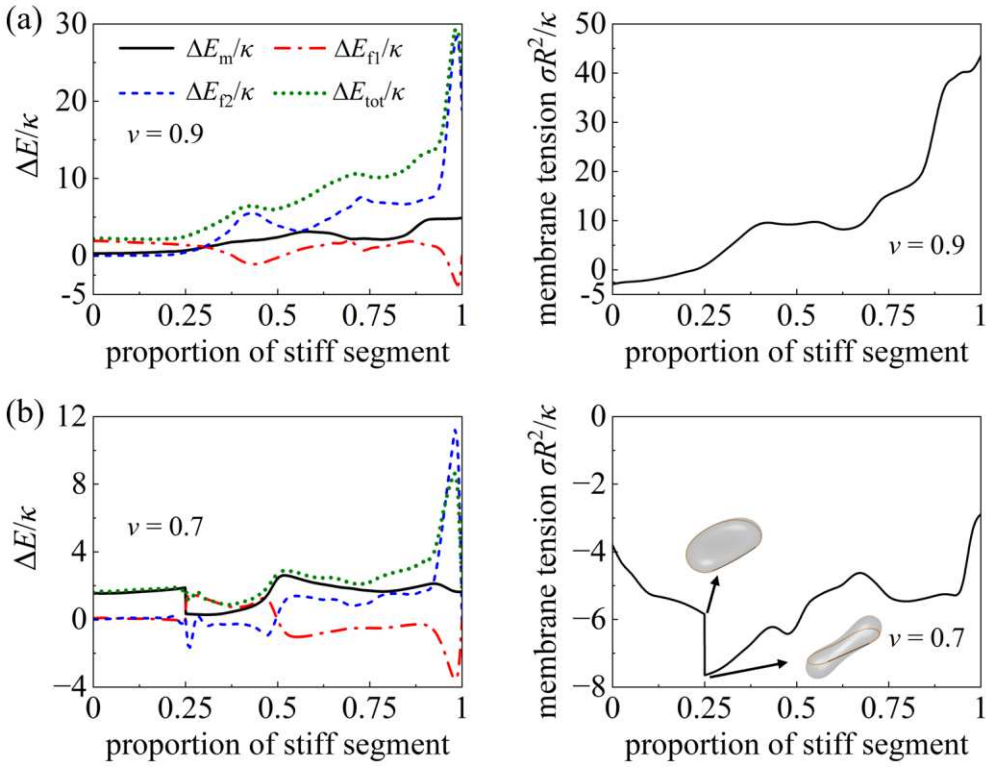

Fig. S3. Energy and membrane tension profiles for the systems with inhomogeneous filaments at v = 0.9 (a) and 0.7 (b). Inset in (c) provides an enlarged view for clarity. Each inhomogeneous filament has two segments, more flexible segment #1 of length L_1 and bending stiffness Y_1I_1 and stiffer segment #2 of length L_2 and bending stiffness Y_2I_2. Here $Y_1I_1/(\kappa R) = 1$, $Y_2I_2/(\kappa R) = 20$, and $L_1 + L_2 = 7.8R$ are taken.